Electronic Supplementary Information: Co-Deposition of Gas Hydrates by Pressurized Thermal Evaporation

Stefan Arzbacher,*[a,d] Nima Rahmatian,[a,b] Alexander Ostermann,[c] Tobias M. Gasser,[d]
Thomas Loerting,[d] and Jörg Petrasch[b]

[a] *illwerke vkw Endowed Professorship for Energy Efficiency, Research Center Energy, Vorarlberg University of Applied Sciences, Hochschulstraße 1, Dornbirn 6850, Austria. E-mail: stefan.arzbacher@fhv.at*
[b] *Department of Mechanical Engineering, Michigan State University, East Lansing, MI, 48824, USA.*
[c] *Department of Mathematics, University of Innsbruck, Technikerstraße 13, Innsbruck 6020, Austria.*
[d] *Institute of Physical Chemistry, University of Innsbruck, Innrain 52c, Innsbruck 6020, Austria.*

Contents

1 Custom-Built Reactor *R-CT*

Fig. S1 shows the experimental setup used for the synthesis of the gas hydrates. This setup is a modified version of the setup described in detail in our recent study of macroscopic defects in decomposing CO_2 clathrate hydrate crystals.[1] The modifications comprise the addition of the graphite rod as well as the graphite crucible at the center of the reactor in order to implement the PTE process described in the main manuscript.

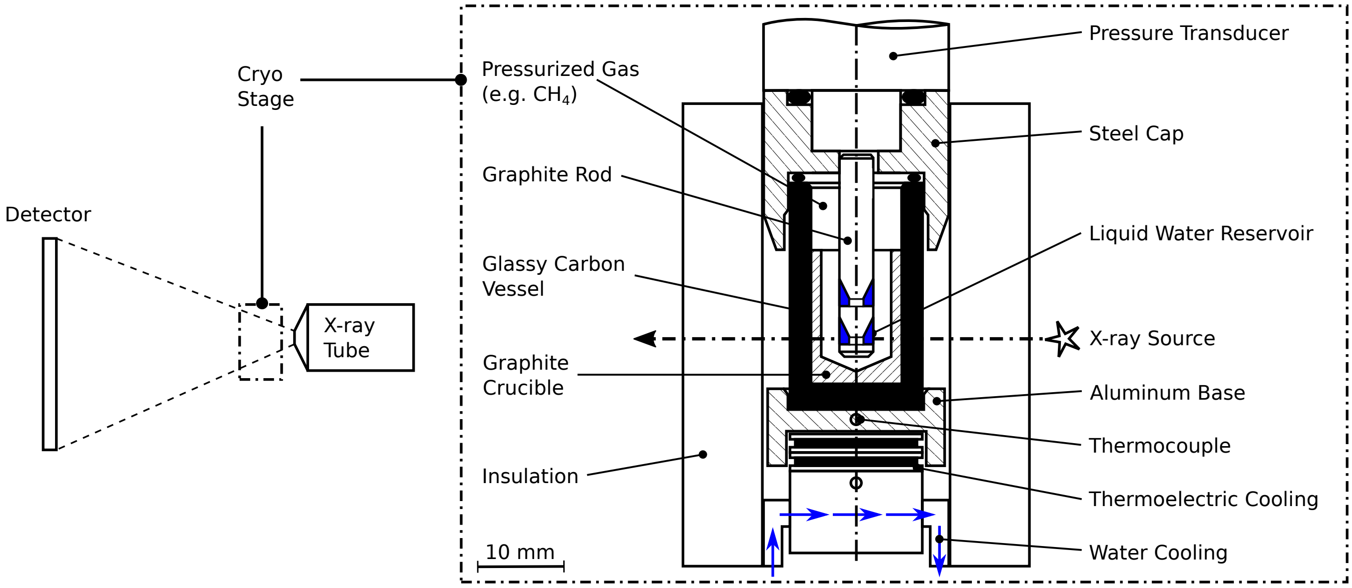

Fig. S1 Schematic of the tomographic setup (left) together with a cross sectional view of the cryo stage (right).

A cryo stage containing the reactor is fixed on the manipulator of a lab-scale micro-computed X-ray tomography (μCT) system (phoenix nanotom-m 180, GE Sensing & Inspection Technologies, Wunstorf, Germany). The reactor consists of a glassy carbon crucible (SIGRADUR G, HTW Germany) and a steel cap fitted together using a two-component epoxy adhesive. An O-ring (PTFE) between the glassy carbon crucible and the steel cap is used to seal the reactor. The bottom of the reactor is in good thermal contact with an aluminum base which is cooled thermoelectrically from below by a stack of Peltier elements (QC-31-1.0-3.9MS and QC-17-1.4-3.7MS, Quick-Ohm Germany). The temperature of the aluminum base is measured with an accuracy of $0.2\,\mathrm{K}$ by a calibrated thermocouple (K-type, $d = 1\,\mathrm{mm}$). Two types of pressure transducers are used and connected to the steel cap of the reactor. A sensor with a range of 0–10 MPa and an accuracy of 8 kPa (PXM459-100BGI, OMEGA Germany) is used for the synthesis experiments. For rapid depressurization experiments, we use a transducer with a range of 0–700 kPa and an accuracy of 0.6 kPa (PXM459-007BGI, OMEGA Germany). The reactor is monitored and controlled using a commercial data acquisition system (NI cRIO-9022, National Instruments USA) at a frequency of 0.1 Hz during synthesis and 1 Hz during rapid depressurization experiments.

1.1 Imaging

All μCT scans are done using the settings specified in Table S1. The 1200 radiographs collected in each μCT scan are used by GE's phoenix datos|x reconstruction software (GE Sensing & Inspection Technologies, Germany) to compute the raw three-dimensional raster image data with a gray scale resolution of 16 bit and a voxel edge length of $6\,\mu$m. A simple three-dimensional median filter with a kernel size of 7 voxels is applied to the raster image data to improve the signal to noise ratio without affecting the level of details (also see ref. 1 for details regarding the image processing). The renderings (2D and 3D) of the filtered image data are created with the software VG Studio MAX 2.2 (Volume Graphics GmbH, Germany) which is also used for the visual inspection of the μCT results.

1.2 Temperature Field in the Reactor

The direct measurement of the temperature field inside the reactor is difficult since the presence of a temperature sensor in the reactor disturbs the temperature field. Particularly, in the case of large temperature gradients and temperature sensors comprising metallic wires, a heat flux along the wire significantly alters the read-out temperature of the sensor. Moreover, in the setting used, metallic wires in the reactor result in metal artefacts in the μCT scans. To avoid these problems, we estimate the temperature field in the reactor using the temperature in the aluminum

Table S1 μCT Scan Parameters

Parameter	Value
Tube Voltage	70 kV
Tube Current	350 μA
Magnification	16.67
Voxel Edge Length	6 μm
Timing	750 ms
Scan Duration	60 min
Average	3
No. of Images	1200

base below the reactor together with computer simulations. The open source 3D multiphysics solver ELMER[2] is applied to solve the conjugate conduction convection problem. The latent heat of evaporation of the water or that of crystallization of the hydrate is neglected in the model. The simulation domain includes the graphite rod, the liquid water reservoir, the pressurized gas, the graphite crucible, the glassy carbon vessel, the steel cap, as well as the insulation. A fixed temperature boundary condition according to the temperature measured at the bottom of the reactor is set at the bottom of the glassy carbon vessel. Similarly, the temperature at the top surface of the steel cap is fixed to the ambient temperature of 295 K. Convective heat transfer to the environment (heat transfer coefficient $h = 22\,\mathrm{W \cdot m^{-2} \cdot K^{-1}}$)[3] is used as the boundary condition at the surface of the insulation. Fig. S2 shows the simulation result for methane at a pressure of 8.0 MPa and a reactor bottom temperature of 258 K. Qualitatively, the simulation result looks the same for carbon dioxide at a pressure of 2.0 MPa and a reactor bottom temperature of 258 K. The simulation results are eventually used to extract estimations for the temperatures $T^\star$, T°, $\Theta^\star$, and Θ° (cf. Fig. S2), which are also used in the main manuscript.

Streamlines, illustrated in the region of the pressurized gas in Fig. S2, show the pathway for water vapor transport by natural convection. Notably, the illustrated flow field matches the distribution of hydrate grown in the synthesis

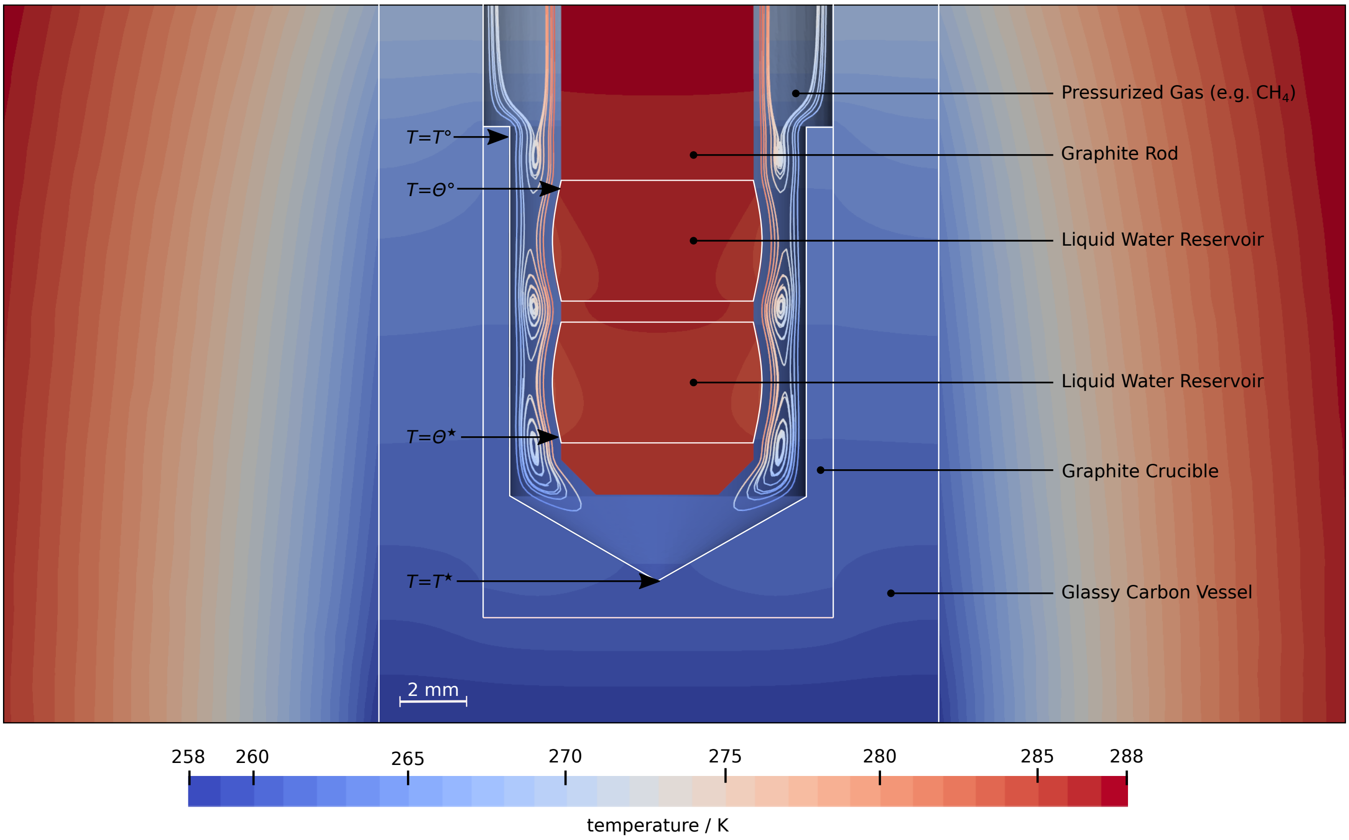

Fig. S2 Temperature profile and natural convection flow in the reactor during the synthesis of CH_4 hydrate at a pressure of 8.0 MPa and a reactor bottom temperature of 258 K. The streamlines in the region of the pressurized gas illustrate the water vapor transport mechanism by convection. The evaporated water rises with the warm gas along the graphite rod, cools down, and falls back along the cold graphite crucible where it is eventually deposited as hydrate.

experiments: most of the hydrate is deposited at the top of the graphite crucible, and essentially no hydrate is deposited at the bottom. This distribution of hydrate can be explained using the three vortices along the cylinder axis which redirect the falling flow of water vapor before it can reach the bottom of the crucible.

2 Thermodynamic Equilibrium Conditions

The choice of hydrate synthesis pressures is determined by the simulated temperatures $T^{\star}$, T° on the hydrate growth site. Dry runs (i.e., experiments with no water in the reactor) are used to ensure that no liquefaction of gas takes place at the p-T conditions chosen. As the liquefaction of the gas or the evaporation of the liquid gas alters the reactor pressure significantly, in dry runs such a change of phase is easily detectable with the pressure sensor. Table S2 lists thermodynamic equilibrium pressures of CO_2 hydrate and CH_4 hydrate as well as vapor pressures of CO_2 at conditions relevant in our synthesis experiments.

Table S2 Thermodynamic equilibrium data[§]

Gas	Temperature (K)	Hydrate Equilibrium Pressure (MPa)	Vapor Pressure (MPa)
CO_2	$\underline{260.5}$	0.65 ± 0.10	2.44 ± 0.01
CO_2	$\underline{265.0}$	0.81 ± 0.06	2.78 ± 0.01
CO_2	278.35 ± 0.25	$\underline{2.3}$	4.00 ± 0.04
CO_2	277.45 ± 0.25	$\underline{2.0}$	3.90 ± 0.02
CO_2	270.70 ± 0.25	$\underline{1.0}$	3.26 ± 0.01
CH_4	$\underline{261.0}$	1.72 ± 0.08	-
CH_4	284.70 ± 1.00	$\underline{7.7}$	-
CH_4	281.90 ± 0.40	$\underline{6.5}$	-

[§] Underlined numbers are fixed values, regularly printed numbers are derived. Hydrate equilibrium pressures and temperatures are based on experimental results summarized in the book of Sloan and Koh[4] and correspond to the values at the liquid water–hydrate–vapor (L–H–V) or the ice–hydrate–vapor (I–H–V) curve. Vapor pressures of CO_2 at the corresponding temperatures are taken from the Dortmund Data Bank.[5]

3 Loading Procedures

3.1 Loading Procedure Reactor *R-CT*

The synthesis of CO_2 and CH_4 hydrate is started outside the reactor by adding deionized liquid water to the grooves of the graphite rod via repeated pipetting (Eppendorf Reference 2, range 0.5–10 μL). We then freeze the water on the graphite rod before it is inserted into the reactor at ambient temperature. Immediately after insertion, the reactor is flushed with the guest gas and subsequently pressurized to the chosen hydrate formation pressure (7.7 MPa for CH_4, 2.3 MPa for CO_2). The usage of frozen water ensures that all water remains on the graphite rod during the loading procedure. After pressurization, the frozen water melts within 5 min due to the warm environment. Melting is evident by the change in the texture of the water as seen in the X-ray radiographs collected at the beginning of the experiment. After the melting of the water is observed, the reactor is cooled and hydrate synthesis is started.

3.2 Loading Procedure Reactor *R-Vis*

We use a pipette (Eppendorf Reference 2, 0.5–10 μL) to add deionized liquid water to the liquid water reservoir while the reactor is at room temperature. For that, the glass cylinder of the reactor has to be removed. After the addition of the water, the glass cylinder is reattached and the reactor tightly closed. Still at room temperature, we then flush the reactor with dry CO_2 gas for approx. 2 min. Subsequently, the reactor is pressurized and cooled to start synthesis.

4 PXRD Experimental Details

The synthesized samples are characterized by powder X-ray diffraction (PXRD). For this, the samples are powdered under liquid nitrogen and transferred to the sample holder of a PheniX Helium Cryostat (Oxford Cryosystems, UK) using a cryospoon. The sample holder is made from copper and precooled to 80 K. After loading the sample at 80 K, it is cooled to 20 K within approximately 10 min and the PXRD measurements are started using a Bruker D8 Advance powder diffractometer equipped with a Cu-Kα1 X-ray source (wavelength $\lambda = 1.5406$ Å) operated at 40 kV and 40 mA in $\Theta/2\Theta$ scanning mode. The first measurement is done at 20 K in the 2Θ range from 5° to 90° with a step width of 0.02° within approximately 75 min. After completion, the sample temperature is raised to 80 K, from where a temperature-resolved crystallographic analysis is started. To this end, a PXRD measurement is done in steps of 5 K in the range from 80 K to 300 K. A smaller 2Θ range of 5° to 55° is used together with a shorter exposure time to limit the scan duration at each temperature step to 5 min. Between two successive measurements, the temperature is raised by approximately $4\,\mathrm{K} \cdot \mathrm{min}^{-1}$. For all PXRD measurements, the chamber is evacuated to below 0.01 mbar. The sample temperature is regulated with a stability of 0.1 K using the temperature controller of the PheniX Cryostat.

5 Complementary Results

Additional results are presented hereafter to complement the findings in the main manuscript.

5.1 Pressure during CO_2 Hydrate Formation in Reactor *R-Vis*

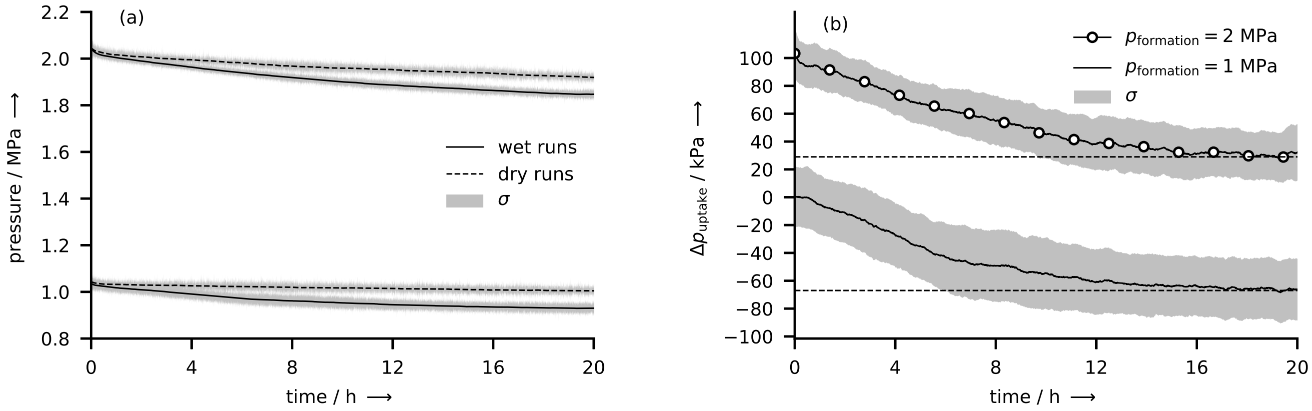

Fig. S3 (a) Absolute pressure in the reactor *R-Vis* during the formation of CO_2 hydrate (labeled "wet run") and during identical experiments with no water loaded (labeled "dry run"). The solid and dashed lines represent the mean pressures $\bar{p}$ derived from five wet and three dry experiments, respectively. The areas filled with gray represent values in the range $[\bar{p} - \sigma, \bar{p} + \sigma]$, where σ denotes the standard deviation of the corresponding set of experiments. (b) Mean pressure drop $\overline{\Delta p}_{\text{uptake}}$ attributed to the uptake of gas by the growing hydrate. The pressure drop is computed by subtracting the mean pressures of the dry runs from those of the wet runs for both, formation experiments at $1\,\mathrm{MPa}$ and $2\,\mathrm{MPa}$. Again, the curves are enveloped by a gray sleeve representing values in the range $[\overline{\Delta p}_{\text{uptake}} - \sigma, \overline{\Delta p}_{\text{uptake}} + \sigma]$. Here, the standard deviation σ is computed by Gaussian error propagation from the uncertainties related to the wet and dry runs. The mean pressure drop associated with the formation pressure of $2\,\mathrm{MPa}$ is shifted by $100\,\mathrm{kPa}$ for better readability.

5.2 *p-T* Data from CO_2 Hydrate Decomposition Experiments in Reactor *R-Vis*

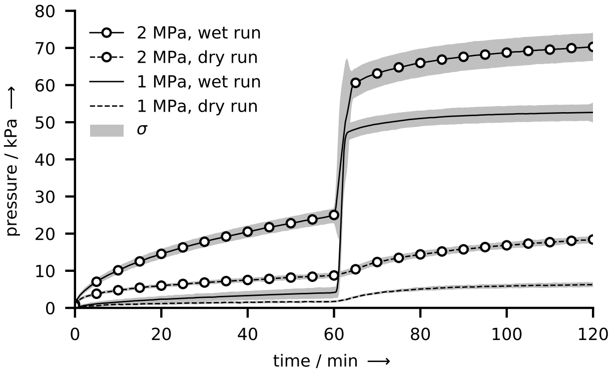

Fig. S4 Gauge pressure in the reactor *R-Vis* during the decomposition of CO_2 hydrate after rapid depressurization (labeled "wet run") and during identical experiments with no water loaded (labeled "dry run"). Note that the dry runs are the same as in Fig. S3. The solid and dashed lines represent the mean pressures $\bar{p}$ derived from five wet and three dry experiments, respectively. The areas filled with gray represent values in the range $[\bar{p} - \sigma, \bar{p} + \sigma]$, where σ denotes the standard deviation of the corresponding set of experiments. The pressure increase observed in dry runs is due to thermal gas expansion as well as due to degassing of CO_2 from the reactor gaskets only. Thermal gas expansion occurs either because the reactor is actively heated or because the gas, which is cooled upon rapid depressurization (i.e., isentropic cooling), rewarms. Both, the effect of isentropic cooling as well as the degassing of dissolved CO_2 are more pronounced in experiments at higher formation pressures. Therefore, in dry runs, the increase in pressure after rapid depressurization is larger for $2\,\mathrm{MPa}$ than for $1\,\mathrm{MPa}$ formation pressure. The difference (cf. Fig. 9 of the main manuscript) between the "wet run" and the "dry run" curve of identical formation pressure eventually yields the pressure increase attributed to the decomposition of the hydrate only. The standard deviations of these difference curves are obtained by Gaussian error propagation from the uncertainties related to the wet and dry runs.

5.3 *p-T* Data from CO_2 Hydrate Rapid Depressurization Experiment

The *p-T* data of the rapid depressurization experiment with a CO_2 hydrate sample in the reactor *R-CT* is shown in Fig. S5.

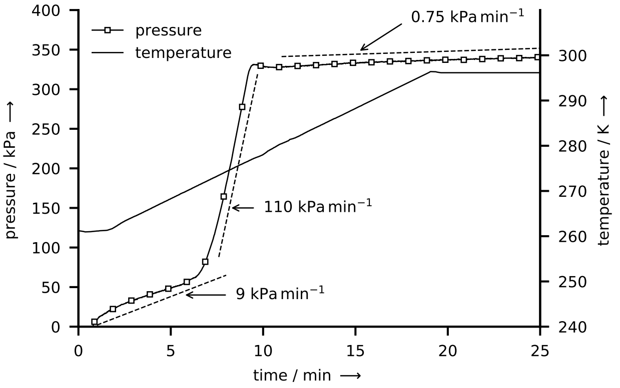

Fig. S5 Gauge pressure and temperature $T^{\star}$ during the decomposition of a CO_2 hydrate sample after rapid depressurization in the reactor *R-CT*. The sample was synthesized from $150\,\mathrm{mg}$ of water using the *p-T* conditions described in the main manuscript.

5.4 Determination of Bulk Water to Gas Molar Ratio from *p-T* Data

The *p-T* data from rapid depressurization experiments are used to determine the molar ratios of water to guest gas. The total mass m_{H_2O} of water in a reactor is determined during the loading procedure with a pipette (Eppendorf Reference 2, 0.5–10$\,\mu$L). At the end of the rapid depressurization experiments both reactors are at room temperature $T_{\text{amb.}}$ and the temperature field is uniform. A small amount $m_{\text{dissolved}}$ of the gas released by the hydrate is dissolved in the liquid water at the temperature $T_{\text{amb.}}$ and reduces the end pressure in the reactors. Hence, the total mass m_{end} of guest gas contained in a reactor with volume V_{reactor} at the end of the experiment can be derived from the absolute pressure p_{end}, the water vapor pressure p_{v}, the compressibility factor $Z_{\text{amb.}}$, and the ideal gas equation:

$$m_{\text{end}} = \frac{(p_{\text{end}} - p_{\text{v}}) \cdot V_{\text{reactor}}}{Z_{\text{amb.}} R T_{\text{amb.}}} + m_{\text{dissolved}}. \tag{S1}$$

In a similar way, we use the absolute pressure $p_{\text{depr.}}$ measured immediately after depressurization to determine the mass of gas $m_{\text{depr.}}$ in a reactor before hydrate decomposition starts. At that time there is no liquid water present and thus no gas dissolved. Note that the water vapor pressure is neglected in the computation of $m_{\text{depr.}}$ because it is not detectable within the accuracy of the pressure sensors at the respective conditions. Since depressurization is done at the temperature $T_{\text{depr.}} < T_{\text{amb.}}$ the temperature field in the reactors is non-uniform (cf. Fig. S2). Nevertheless, for an average temperature T_x with $T_{\text{depr.}} \leq T_x \leq T_{\text{amb.}}$ the mass $m_{\text{depr.}}$ is bounded by

$$\frac{p_{\text{depr.}} \cdot V_{\text{reactor}}}{R T_{\text{amb.}}} \leq m_{\text{depr.}} = \frac{p_{\text{depr.}} \cdot V_{\text{reactor}}}{R T_x} \leq \frac{p_{\text{depr.}} \cdot V_{\text{reactor}}}{R T_{\text{depr.}}}. \tag{S2}$$

Note that the use of a compressibility factor Z is omitted here since $Z \approx 1.00$ for both CH_4 and CO_2 at the *p-T* conditions immediately after depressurization. Hence, a lower bound m^{-}_{gas} of the mass of released gas m_{gas} (i.e., the mass of gas contained in the sample) is given by

$$m^{-}_{\text{gas}} = \frac{V_{\text{reactor}}}{R} \cdot \left(\frac{p_{\text{end}} - p_{\text{v}}}{Z_{\text{amb.}} T_{\text{amb.}}} - \frac{p_{\text{depr.}}}{T_{\text{depr.}}} \right) + m_{\text{dissolved}} \leq m_{\text{end}} - m_{\text{depr.}} = m_{\text{gas}}, \tag{S3}$$

and an upper bound by

$$m^{+}_{\text{gas}} = \frac{V_{\text{reactor}}}{R} \cdot \left(\frac{p_{\text{end}} - p_{\text{v}}}{Z_{\text{amb.}} T_{\text{amb.}}} - \frac{p_{\text{depr.}}}{T_{\text{amb.}}} \right) + m_{\text{dissolved}} \geq m_{\text{end}} - m_{\text{depr.}} = m_{\text{gas}}. \tag{S4}$$

Using the molar masses of water and guest gas, an upper bound n^{+} and lower bound n^{-} to the molar ratio of water to gas (i.e., n_{H_2O}/n_{gas}) then follows directly from m_{H_2O} as well as m^-_{gas} and m^+_{gas}, respectively:

$$n^+ = \frac{m_{H_2O}}{m^-_{gas}} \cdot \frac{M_{gas}}{M_{H_2O}} \geq \frac{m_{H_2O}}{m_{gas}} \cdot \frac{M_{gas}}{M_{H_2O}} = \frac{n_{H_2O}}{n_{gas}} \geq \frac{m_{H_2O}}{m^+_{gas}} \cdot \frac{M_{gas}}{M_{H_2O}} = n^- . \tag{S5}$$

Table S3 and S4 summarize symbols as well as the original and the derived experimental data used for the determination of n^+ and n^-.

Table S3 Original and derived data with uncertainties for the experiments in reactor *R-CT*

Symbol	Description	Value in CH_4 synthesis experiment	Value in CO_2 synthesis experiment
m_{H_2O}	total mass of water in the reactor	(50.0 ± 0.5) mg	(150.0 ± 1.5) mg
$m_{depr.}$	gas mass in the reactor before decomposition starts	(5.72 ± 0.66) mg	(16.07 ± 1.16) mg
m_{end}	gas mass in the reactor after decomposition at room temperature $T_{amb.}$	(11.9 ± 0.2) mg	(67.6 ± 1.1) mg
$m_{dissolved}$	mass of gas dissolved in water‡	$(2.5 \pm 0.3)\,\mu$g	(1.09 ± 0.11) mg
m^-_{gas}	lower bound of released gas	(5.6 ± 0.2) mg	(50.6 ± 0.9) mg
m^+_{gas}	upper bound of released gas	(6.8 ± 0.2) mg	(52.4 ± 0.9) mg
$V_{reactor}$	total gas volume of the reactor	(8.2 ± 0.1) mL	(8.2 ± 0.1) mL
$p_{depr.}$	absolute reactor pressure before decomposition starts	(96.6 ± 0.6) kPa	(102.1 ± 0.6) kPa
p_{end}	absolute reactor pressure after decomposition at room temperature $T_{amb.}$	(225.0 ± 0.6) kPa	(442.0 ± 0.6) kPa
p_v	water vapor pressure§ at $T_{amb.}$	3.169 kPa	2.339 kPa
$T_{amb.}$	room temperature	(298.0 ± 0.5) K	(293.0 ± 0.5) K
$T_{depr.}$	temperature $T^\star$ (cf. Fig. S2) before decomposition starts	(243 ± 1) K	(261 ± 1) K
$Z_{amb.}$	gas compressibility factor¶ at $T_{amb.}$ and p_{end}	0.99 ± 0.01	0.98 ± 0.01
n^-	lower bound of the bulk water to gas molar ratio	6.58 ± 0.16	6.99 ± 0.14
n^+	upper bound of the bulk water to gas molar ratio	7.94 ± 0.23	7.25 ± 0.15

‡ Gas dissolution is computed on the basis of Bunsen coefficients reported by Wiesenburg et al.[6] for CH_4 and Bartholomé et al.[7] for CO_2.

§ Vapor pressures taken from the steam tables of Moore et al.[8]

¶ The gas compressibility factor is derived using critical pressure and temperature as well as the generalized compressibility chart.

Table S4 Original and derived data with uncertainties for the experiments in reactor *R-Vis*

Symbol	Description	Value for 1 MPa synthesis pressure experiment set	Value for 2 MPa synthesis pressure experiment set
m_{H_2O}	total mass of water in the reactor	(100.0 ± 1.0) mg	(100.0 ± 1.0) mg
$m_{depr.}$	gas mass in the reactor before decomposition starts	(36.15 ± 3.75) mg	(36.15 ± 3.70) mg
m_{end}	gas mass in the reactor after decomposition at room temperature $T_{amb.}$	(50.2 ± 2.7) mg	(52.1 ± 3.0) mg
$m_{dissolved}$	mass of gas dissolved in water‡	(0.23 ± 0.02) mg	(0.24 ± 0.03) mg
m^-_{gas}	lower bound of released gas	(12.2 ± 1.1) mg	(14.2 ± 1.6) mg
m^+_{gas}	upper bound of released gas	(16.1 ± 1.2) mg	(18.0 ± 1.7) mg
$V_{reactor}$	total gas volume of the reactor	(19.00 ± 0.95) mL	(19.00 ± 0.95) mL
$p_{depr.}$	absolute reactor pressure before decomposition starts	(100.0 ± 1.0) kPa	(100.0 ± 1.0) kPa
p_{end}	absolute reactor pressure after decomposition at room temperature $T_{amb.}$	(146.2 ± 2.2) kPa	(151.8 ± 3.8) kPa
p_v	water vapor pressure§ at $T_{amb.}$	2.645 kPa	2.645 kPa
$T_{amb.}$	room temperature	(295.0 ± 0.5) K	(295.0 ± 0.5) K
$T_{depr.}$	temperature $T^\star$ (cf. Fig. S2) before decomposition starts	(265.0 ± 0.2) K	(265.0 ± 0.2) K
$Z_{amb.}$	gas compressibility factor¶ at $T_{amb.}$ and p_{end}	0.98 ± 0.01	0.98 ± 0.01
n^-	lower bound of the bulk water to gas molar ratio	15.2 ± 1.2	13.5 ± 1.3
n^+	upper bound of the bulk water to gas molar ratio	20.0 ± 1.9	17.2 ± 2.0

‡ Gas dissolution is computed on the basis of Bunsen coefficients reported by Wiesenburg et al.[6] for CH_4 and Bartholomé et al.[7] for CO_2.

§ Vapor pressures taken from the steam tables of Moore et al.[8]

¶ The gas compressibility factor is derived using critical pressure and temperature as well as the generalized compressibility chart.

5.5 Crystallographic Data Analysis

The PXRD profiles measured at 20 K are analyzed using the software GSAS-II[9] to determine the phase mixture of hexagonal ice and structure I hydrate. The crystal structure refinement is done in the 2Θ range from 10° to 80° since no intense Bragg peaks are found at both lower and higher angles. The crystallographic structure files for the individual phases are taken from Röttger et al.[10] (ice Ih), Falenty et al.[11] (sI hydrate CO_2), and Gutt et al.[12] (sI hydrate CH_4). The crystal lattice constants as well as the phase fractions are refined together with the instrument parameters while the atomic positions of the individual phases are fixed. Fig. S6 shows the result of the refinement for the CO_2 and the CH_4 hydrate sample. Table S5 lists the key data of the refined crystal structure.

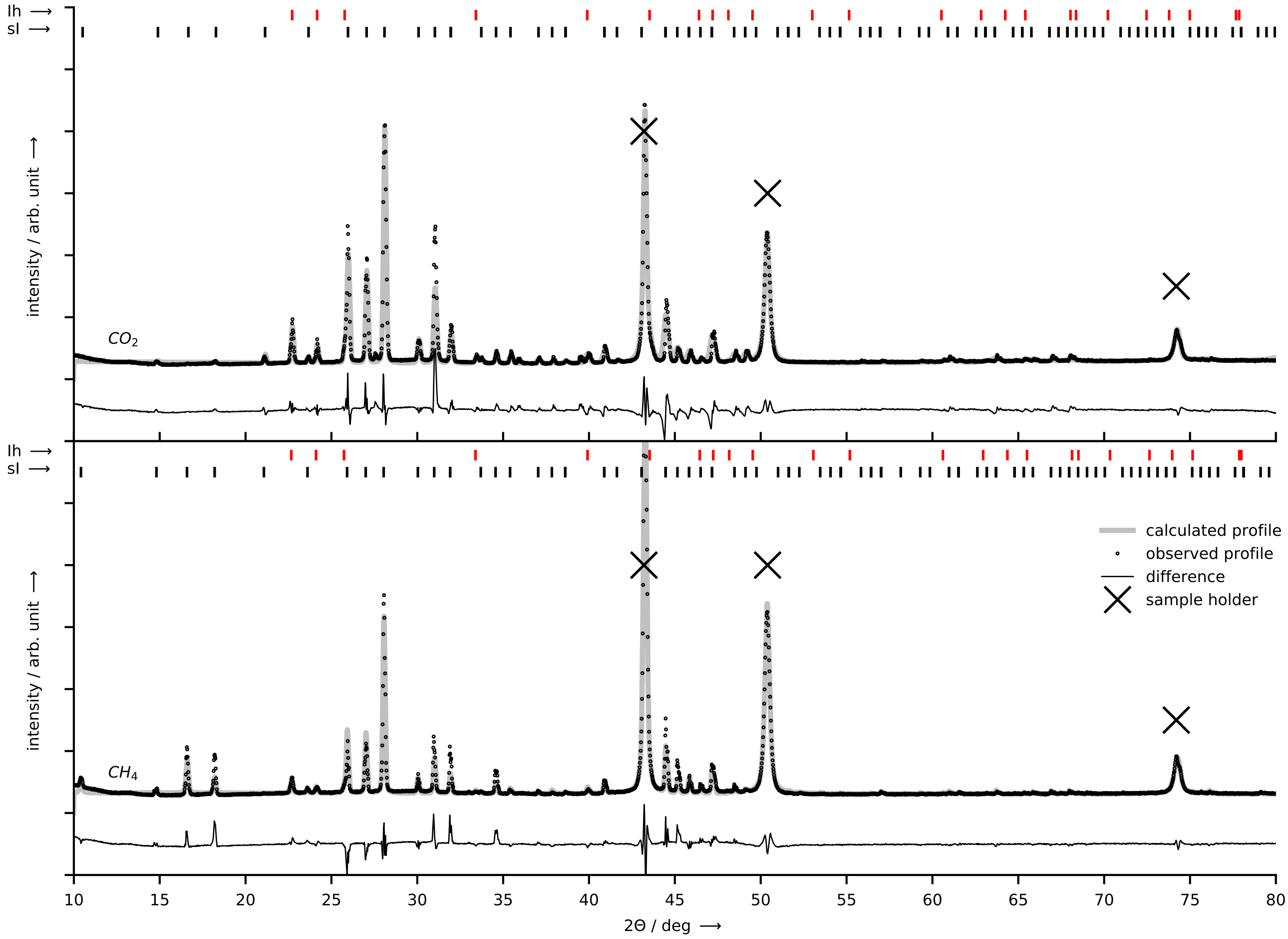

Fig. S6 Observed and calculated PXRD profile of the CO_2 (top) and the CH_4 hydrate sample (bottom). The observed profiles stem from the PXRD measurements done at 20 K with Cu-Kα1 radiation ($\lambda = 1.5406$ Å). Bragg peaks marked with an "X" originate from the copper sample holder. Tick marks at the top of the graphs denote Bragg reflections caused by the cubic structure I hydrate (sI, black) or the hexagonal ice (Ih, red).

Table S5 Result of the crystal structure analysis

sample	lattice parameters sI ($a, b, c, \alpha, \beta, \gamma$)	lattice parameters sI ($a, b, c, \alpha, \beta, \gamma$)	mass fraction sI hydrate	mass fraction ice Ih	weighted R-factor
CO_2 hydrate	11.867, 11.867, 11.867, 90, 90, 90	4.513, 4.513, 7.353, 90, 90, 120	0.927 ± 0.007	0.073 ± 0.002	11.86 %
CH_4 hydrate	11.837, 11.837, 11.837, 90, 90, 90	4.521, 4.521, 7.362, 90, 90, 120	0.937 ± 0.009	0.063 ± 0.004	8.85 %

5.6 Temperature-Resolved PXRD Results

Temperature-resolved PXRD measurements in the range from 80 K to 300 K are done with both hydrate samples in steps of 5 K to study differences in the decomposition behavior of the CO_2 and CH_4 hydrate. One step in temperature involves a 1 min temperature ramp followed by a 5 min measurement period at constant temperature. Figure S6 shows the normalized peak areas of four ice (Ih) and three hydrate (sI) Bragg peaks as a function of temperature for both CO_2 and CH_4 hydrate. Fig. S8 shows the peak intensity ratios of a few selected Bragg peaks as a function of temperature. The peak intensity ratios are computed by dividing the normalized Bragg peak areas shown in Fig. S7. The selected peaks correspond to the hexagonal ice (Ih) reflections of the 100 (Ih100), 002 (Ih002), 110 (Ih110), and 102 (Ih102) crystallographic planes. While the Ih100 and Ih102 reflections do not overlap with reflections caused by cubic ice (Ic) an overlap exists for Ih002 (with Ic111) and Ih110 (with Ic220).

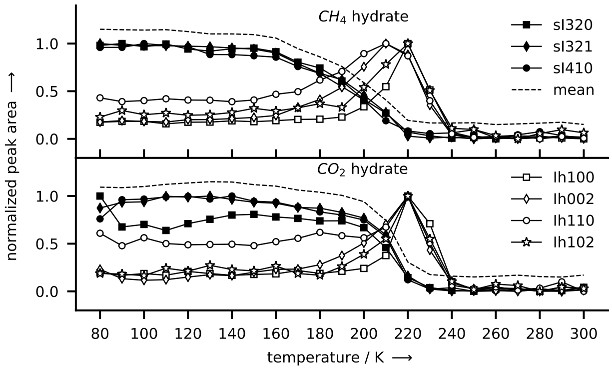

Fig. S7 Normalized Bragg peak area of four hexagonal ice (labelled Ih) and three crystal structure I (labelled sI) reflexes as a function of temperature. The peak areas are obtained from temperature-resolved PXRD measurements with CH_4 hydrate (top) and CO_2 hydrate (bottom) in the temperature range from $80\,\mathrm{K}$ to $300\,\mathrm{K}$ in steps of $5\,\mathrm{K}$. The dashed line is the mean value of the sI curves shifted by 0.15 for better readability.

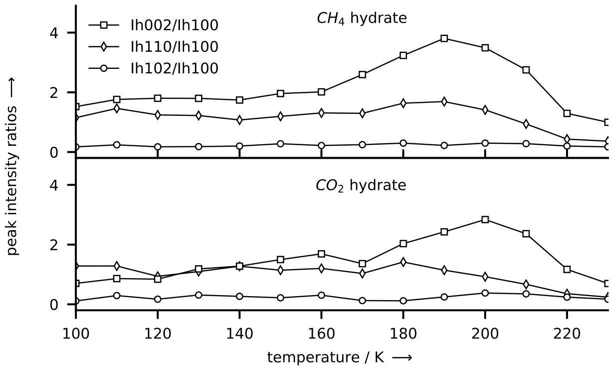

Fig. S8 Peak intensity ratios of selected Bragg peaks as a function of temperature. The ratios are calculated by dividing normalized Bragg peak areas obtained from temperature-resolved PXRD measurements done with the CH_4 (top) and the CO_2 hydrate sample (bottom).

It is evident that with increasing temperature, the Bragg peaks of ice grow while the Bragg peaks of hydrate vanish. The CH_4 hydrate sample starts to decompose at a slow rate at roughly $160\,\mathrm{K}$. In the case of CO_2 hydrate, decomposition begins at about $180\,\mathrm{K}$. In both cases the Bragg peaks of ice grow differently during the decomposition of the hydrates. For instance, the Ih002 peak increases immediately after the onset of decomposition while the Ih100 peak remains constant up to higher temperatures. This results in an increased intensity ratio of the Ih002 and Ih100 peak in the range 170–$220\,\mathrm{K}$ (see Fig. S8) and indicates the formation of defective cubic ice (Ic) instead of hexagonal ice upon hydrate decomposition.[13–15] At temperatures above 200 K the defective ice starts to anneal and the Ih002/Ih100 ratio decreases. In both samples, at $220\,\mathrm{K}$ all hydrate transforms into ice, which itself sublimates at 220–$250\,\mathrm{K}$ due to the vacuum ($p < 0.01\,\mathrm{mbar}$) of the diffractometer.

5.7 Co-Deposited Hydrate Film before Rapid Depressurization

A photo of a newly deposited layer of CO_2 hydrate is shown in Fig. S9. The depicted hydrate was formed in the reactor *R-Vis* and later used in the series of rapid depressurization experiments discussed in the main manuscript.

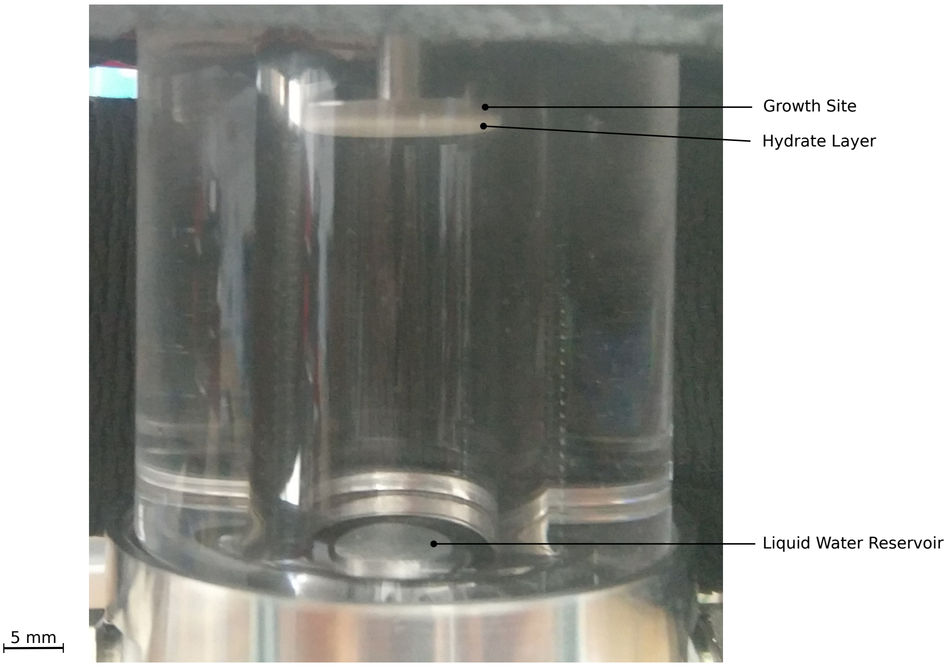

Fig. S9 CO_2 hydrate layer co-deposited on an aluminum growth site of the reactor *R-Vis*. At the end of hydrate synthesis no water is left in the liquid water reservoir formed by an aluminum disk. Moreover, any fog on the interior glass walls vanishes. Temperatures are $265\,\mathrm{K}$ on the growth site and $265\,\mathrm{K}$ on the liquid water reservoir. Based on the known mass of water and the surface area of the growth site, we estimate the thickness of the hydrate to be $330\,\mu\mathrm{m}$.

5.8 μCT Tomograms (2D) of CH_4 Hydrate Synthesis

The 3D illustrations presented in the main manuscript are based on stacks of tomograms. One vertical and two horizontal tomograms of the CH_4 hydrate synthesis experiment are depicted for different times at identical positions in Fig. S3 to show the size of the hydrate crystals. Note that the morphology of the hydrate crystals obtained from the CO_2 hydrate synthesis experiment is identical to that shown in Fig. S10.

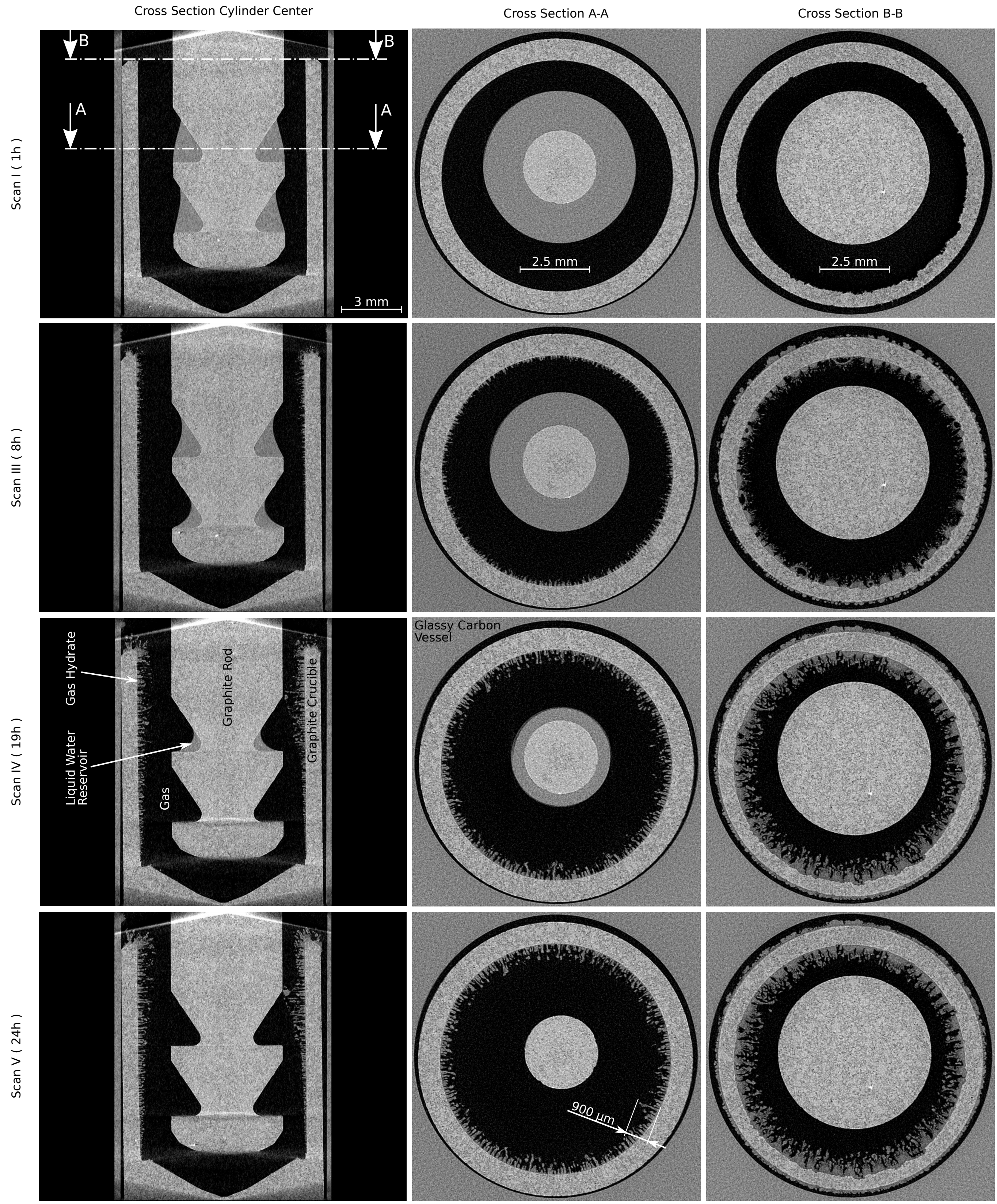

Fig. S10 μCT tomograms at identical positions of the reactor at four different times in the CH_4 hydrate synthesis experiment. The scan numbers refer to the labels in Fig. 4 of the main manuscript. All tomograms have been processed using a median filter with a kernel size of 7 voxels (also see ref. 1 for details regarding the image processing).

References

1 S. Arzbacher, N. Rahmatian, A. Ostermann, B. Massani, T. Loerting and J. Petrasch, *Phys. Chem. Chem. Phys.*, 2019, **21**, 9694 – 9708.

2 P. Råbak, M. Malinen, J. Ruokolainen, A. Pursula and T. Zwinger, *Elmer Models Manual*, CSC–IT Center for Science, Helsinki, Finland, 2013.

3 *Principles of Heat and Mass Transfer*, ed. F. P. Incropera, D. P. DeWitt, T. L. Bergman and A. S. Lavine, Wiley, Singapore, 7th edn, 2013.

4 E. D. Sloan and C. A. Koh, *Clathrate Hydrates of Natural Gases, Third Edition*, CRC Press, 2007.

5 *Dortmund Data Bank, www.Ddbst.Com*, 2019.

6 D. A. Wiesenburg and N. L. Guinasso, *J. Chem. Eng. Data*, 1979, **24**, 356–360.

7 E. Bartholomé and H. Friz, *Chem. Ing. Tech.*, 1956, **28**, 706–708.

8 J. Moore, F. Keyes, J. Keenan and P. Hill, *Steam Tables. Thermodynamic Properties of Water Including Vapor, Liquid, and Solid Phases*, John Wiley & Sons, Inc.: New York, 1969.

9 B. H. Toby and R. B. Von Dreele, *J. Appl. Crystallogr.*, 2013, **46**, 544–549.

10 K. Röttger, A. Endriss, J. Ihringer, S. Doyle and W. F. Kuhs, *Acta Crystallogr., Sect. B: Struct. Sci.*, 1994, **50**, 644–648.

11 A. Falenty, A. N. Salamatin and W. F. Kuhs, *J. Phys. Chem. C*, 2013, **117**, 8443–8457.

12 C. Gutt, B. Asmussen, W. Press, M. R. Johnson, Y. P. Handa and J. S. Tse, *J. Chem. Phys.*, 2000, **113**, 4713–4721.

13 A. Falenty and W. F. Kuhs, *J. Phys. Chem. B*, 2009, **113**, 15975–15988.

14 W. F. Kuhs, G. Genov, D. K. Staykova and T. Hansen, *Phys. Chem. Chem. Phys.*, 2004, **6**, 4917–4920.

15 T. L. Malkin, B. J. Murray, C. G. Salzmann, V. Molinero, S. J. Pickering and T. F. Whale, *Phys. Chem. Chem. Phys.*, 2015, **17**, 60–76.